

The 21 cm Forest as a Probe of the Reionization and the Temperature of the Intergalactic Medium

Yidong Xu^{1,2}, Xuelei Chen², Zuhui Fan¹, Hy Trac³, and Renyue Cen⁴

ABSTRACT

Using high redshift radio sources as background, the 21 cm forest observations probe the neutral hydrogen absorption signatures of early structures along the lines of sight. Directly sensitive to the spin temperature of the hydrogen atoms, it complements the 21 cm tomography observations, and provides information on the temperature as well as the ionization state of the intergalactic medium (IGM). We use a radiative transfer simulation to investigate the 21 cm forest signals during the epoch of reionization. We first confirmed that the optical depth and equivalent width (EW) are good representations of the ionization and thermal state of the IGM. The features selected by their relative optical depth are excellent tracers of ionization fields, and the features selected by their absolute optical depth are very sensitive to the IGM temperature, so the IGM temperature information could potentially be extracted from 21 cm forest observation, thus breaking a degeneracy in 21 cm tomographic observation. With the EW statistics, we predict some observational consequences for 21 cm forest. From the distributions of EWs and the number evolution of absorbers and leakers with different EWs, we see clearly the cosmological evolution of ionization state of the IGM. The number density of potentially observable features decreases rapidly with increasing gas temperature. The sensitivity of the proposed EW statistic to the IGM temperature makes it a unique and potentially powerful probe of reionization. Missing small-scale structures, such as small filaments and minihalos that are unresolved in our current simulation, and lack of an accurate calculation of the IGM temperature, however, likely have rendered the presented signals quantitatively inaccurate. Finally we discuss the requirements of the background radio sources for such observations, and find that signals with equivalent widths larger than 1kHz are hopeful to be detected.

Subject headings: cosmology: theory — intergalactic medium — quasars: absorption lines

¹Department of Astronomy, School of Physics, Peking University, Beijing 100871, China

²National Astronomical Observatory of China, CAS, Beijing 100012, China

³Harvard-Smithsonian Center for Astrophysics, Harvard University, 60 Garden St., Cambridge MA, 02138, USA

⁴Department of Astrophysical Sciences, Princeton University, Princeton, New Jersey 08544, USA

1. Introduction

The reionization of the intergalactic medium (IGM) is one of the landmark events in the history of the universe. While a lot of theoretical works (Wyithe & Loeb 2003; Furlanetto et al. 2004b; Zhang et al. 2007; Choudhury & Ferrara 2007; Choudhury 2009, e.g.) and observational constraints (Fan et al. 2006; Dunkley et al. 2008; Gallerani et al. 2008, e.g.) have sketched up a global picture of the reionization process, many detailed issues remain uncertain (Ciardi & Ferrara 2005). One of the most promising probes of the cosmic reionization is the redshifted 21 cm transition of HI (see e.g. Furlanetto et al. 2006 for a review). The emission or absorption of the 21 cm radiation is directly related to the neutral component of the IGM at different redshifts, thus affording us the most clear view of the reionization history. Moreover, unlike the Ly α resonance line which also traces the neutral hydrogen, the 21 cm line has an extremely small Einstein coefficient ($A_{10} = 2.85 \times 10^{-15} \text{ s}^{-1}$), hence it is not saturated even at high redshift, and one can therefore safely predict the neutral fraction from its 21 cm optical depth.

The most commonly discussed way of 21 cm observation is *21 cm tomography*, in which the three dimensional structure of the emission or absorption of 21 cm photons by the IGM against the CMB is observed (Madau et al. 1997; Tozzi et al. 2000; Iliev et al. 2002; Furlanetto et al. 2004b,c). A less frequently discussed way of 21 cm observation is to observe the spectra of high redshift radio point sources, such as quasars or gamma ray burst (GRB) radio afterglows, and look for absorption or leak features produced by structures along the line of sight. Such *21 cm forest* could be produced by structures of different scales, including the large scale HI/HII regions (“bubbles”), the cosmic web, proto-galaxies or mini-halos. The optical depth of the 21 cm line due to the absorption by the IGM at redshift z is (Field 1959; Madau et al. 1997; Furlanetto et al. 2006):

$$\begin{aligned} \tau_{\nu_0}(z) &= \frac{3}{32\pi} \frac{h_p c^3 A_{10}}{k_B \nu_0^2} \frac{x_{HI} n_H(z)}{T_S (1+z) (dv_{\parallel}/dr_{\parallel})} \\ &\approx 0.009(1+\delta)(1+z)^{3/2} \frac{x_{HI}}{T_S} \left[\frac{H(z)/(1+z)}{dv_{\parallel}/dr_{\parallel}} \right], \end{aligned} \quad (1)$$

where x_{HI} is the neutral fraction of hydrogen at a specific position, $n_H(z)$ and T_S are the number density of hydrogen and the spin temperature of the IGM at that position, respectively, and $dv_{\parallel}/dr_{\parallel}$ is the gradient of the proper velocity along the line of sight, including both the Hubble expansion and the peculiar velocity. As we are going to study the large scale HI/HII regions, the peculiar velocity is neglected. In the second line, the factor $(1+\delta)$ is the overdensity of the baryons, and T_S is in units of Kelvin.

In the following, we will assume that the spin temperature always follows the gas temperature, i.e. $T_S = T_K$. This is a good approximation for the redshifts relevant here (Santos et al. 2008), where the Ly α background from star formations (Madau et al. 1997; Chen & Miralda-Escudé 2004) is present, and the HI spin temperature is strongly coupled to the kinetic temperature via the Wouthuysen-Field effect (Wouthuysen 1952; Field 1959). The 21 cm forest signal is sensitive to the spin temperature, this is a great advantage compared with 21 cm tomographic observation

against the CMB background. The latter could also be sensitive to the spin temperature in the case of absorption, but once the spin temperature raises above the CMB temperature, the 21 cm signal become emission, which saturates and become almost independent of T_S . This uncertainty in spin temperature causes large degeneracies between cosmological and astrophysical parameters in 21 cm tomography (Santos & Cooray 2006). The information extracted from the 21 cm forest observation may help us to determine the spin temperature at the relevant redshifts, and reduce the degeneracies in 21 cm tomography.

Carilli et al. (2002) used numerical simulation to illustrate the 21 cm forest imprinted on quasar spectrum. Furlanetto & Loeb (2002) considered small scale features produced by mini-halos and galaxies. The absorption features produced by the HII regions (“ionized bubbles”) before reionization was studied (Furlanetto 2006; Xu 2006) using the analytical “bubble model” of reionization (Furlanetto et al. 2004b,c), in which the ionization proceeds inside-out, i.e. from high density regions to low density regions.

The reionization process is very complicated, although the “bubble model” picture of reionization is in general agreement with simulation results (Zahn et al. 2007; Iliev et al. 2007; Mellema et al. 2006; Trac & Cen 2007; Shin, Trac & Cen 2008), the complicated geometry of the ionized regions is not considered in this simple analytical model. Therefore, to extract information from future 21 cm forest observations, it is imperative to examine how the 21 cm forest observables are correlated with the reionization process by using numerical simulations. In this paper, we study the large scale 21 cm forest produced by the neutral and ionized bubbles using the reionization simulation by Shin, Trac & Cen (2008). The high resolution simulation has detailed modeling of star formation and radiative transfer of ionizing photons. First, we check whether the equivalent width (EW) can be a representative indicator of the ionization and thermal state of the IGM, and to what extent the 21 cm forests trace cosmic reionization. Then we use simulation data to predict the observational consequences for 21 cm forest. Comparing them with realistic parameters of radio arrays, we study what constraints we could put on reionization from 21 cm forest observations.

We briefly describe the reionization simulation in section 2. In section 3, we check whether or not, and to what extent, the optical depth (hence the equivalent width) follows the ionization state x_i , density field ρ , and thermal history T_{IGM} of the IGM. From these analyses, we would see what information can be extracted from EW statistics. Then we predict the 21 cm forest signals – distributions and evolution of EWs – from the reionization simulation in section 4. In section 5 we investigate whether there are sufficient number of background sources that are luminous enough for such 21 cm forest observations. We summarize and discuss our results in section 6.

Throughout the paper we use the same Λ CDM cosmology as Shin, Trac & Cen (2008) based on the WMAP3 results (see Spergel et al. 2007, and references therein): $(\Omega_m, \Omega_\Lambda, \Omega_b, h, \sigma_8, n_s) = (0.26, 0.74, 0.044, 0.72, 0.77, 0.95)$.

2. The Simulation

In this paper, we use the reionization simulation described in detail in Shin, Trac & Cen (2008). The high-resolution simulation was run using a hybrid code that contains a N-body algorithm for dark matter, prescriptions for baryons and star formation, and a radiative transfer algorithm for ionizing photons. All components are solved simultaneously in a periodic box with comoving side length of 100 Mpc/h.

The N-body calculations included 2880^3 collisionless dark matter particles, each with a mass of $3.02 \times 10^6 M_\odot/h$. This provided sufficient resolution to resolve halos down to masses of $\sim 10^8 M_\odot/h$ and account for the majority of photo-ionizing sources. For each particle, the local matter density and velocity dispersion are calculated in order to model the baryons and star formation. The baryons are assumed to have the same overdensity field as the dark matter, and the temperature field is set by the velocity dispersion of the particles. Radiative heating and cooling of the gas are not included in the hybrid simulation.

The criterion for star formation was that the particles must have densities $\rho_m > 100\rho_{crit}(z)$ and temperatures $T > 10^4$ K. This cut in the temperature-density phase space effectively restricts star formation to regions within the virial radius of halos that cool efficiently through atomic line transitions. The simulation distinguishes between the first generation, Population III (Pop III) stars and the second generation, Population II (Pop II) stars. The stellar initial mass function is determined by following the metallicity enrichment of the halo and the IGM as described in Trac & Cen (2007). The input spectrum for ionizing radiation is divided in three energy ranges (eV): $13.61 \leq \nu < 24.59$, $24.59 \leq \nu < 54.42$, and $\nu \geq 54.42$, according to the ionization limits for HI, HeI, and HeII.

The radiative transfer algorithm for ionizing radiation is based on a photon-advection scheme that is computationally much less expensive than the ray-tracing scheme in Trac & Cen (2007). These two approaches have been demonstrated to give very similar results for the majority of the reionization epoch (Shin, Trac & Cen 2008). In the hybrid simulation, reionization is completed by $z \approx 6$. For post-analysis, the dark matter, baryons, and radiation are collected on a grid with 720^3 cells and the data is saved every 10 million years from $z = 25$ down to $z = 5$. In this paper, we make use of the gas density, ionization, and temperature fields.

We mark a cell as “ionized” if the ionization fraction is greater than 0.5, and “neutral” otherwise. Slices of ionization field for several redshifts are shown in Fig. 1. Each slice in the figure has a thickness of 139 kpc/h, and this applies to all the other slice-plots in the following. We see that the HII bubbles were highly biased and non-spherical; the universe became 50% ionized at redshift $z \sim 9.5$, and the non-gaussianity in the HII field was significant throughout the reionization. In addition, the simulation also shows that Pop III galaxies played a very important role in the process, and a strong correlation existed between halo number density and bubble size for large bubbles.

To characterize the ionized region statistically, we use the Friend-of-Friend (FoF) algorithm

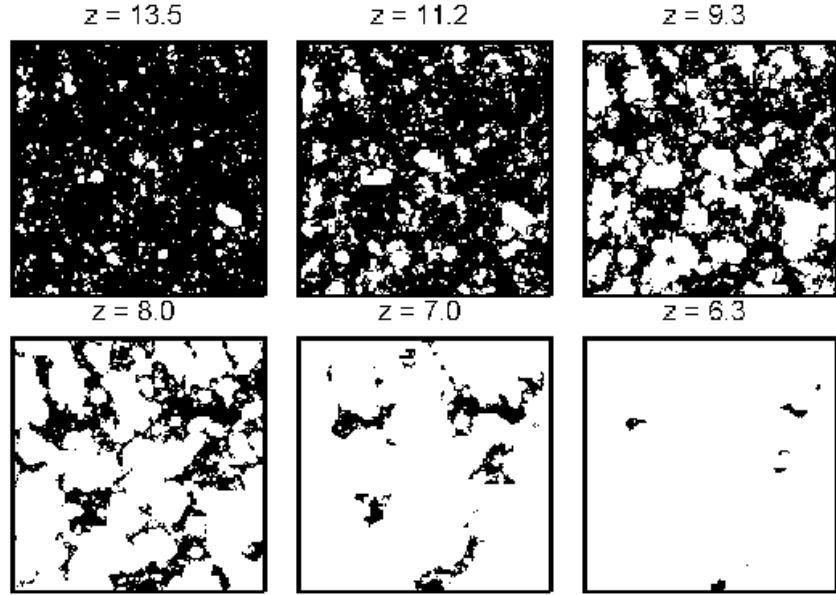


Fig. 1.— Distributions of ionization fraction at redshifts $z \sim 13.5, 11.2, 9.3, 8.0, 7.0$, and 6.3 . Highly ionized regions are represented by white while regions with ionization fraction below 50 percent is shown as black. These are plots of slices in the simulation box with each side of 100 Mpc/h. The global ionization fractions are $\sim 0.094, 0.24, 0.46, 0.73, 0.91$, and 0.98 respectively.

to select ionized bubbles (introduced by Iliev et al. (2006)), which are made of connected ionized cells. The linking length is set to be 1.2 times the simulation data output cell size, so that cells are connected by one face at least. In addition, one bubble consists of 2 or more connected cells. Fig. 2 shows the size distributions of bubbles selected by ionized fraction (x_i -bubbles), with $x_i \geq 0.5$, at several redshifts. As discovered by Shin, Trac & Cen (2008), before the percolation of the ionization bubbles, these ionized-fraction-selected bubbles (x_i -bubbles) have the distributions with three distinct peaks. The characteristic volumes for the three peaks are $0.6, 0.03$, and 0.006 Mpc 3 /h 3 respectively. These sizes do not change significantly with decreasing redshift, before one connected network of bubbles dominated at $z \leq 10$. The smallest peak in each distribution is due to limited resolution of the simulation (i.e. cell size). The other two characteristic sizes are believed to be real features of the size distribution (Shin, Trac & Cen 2008).

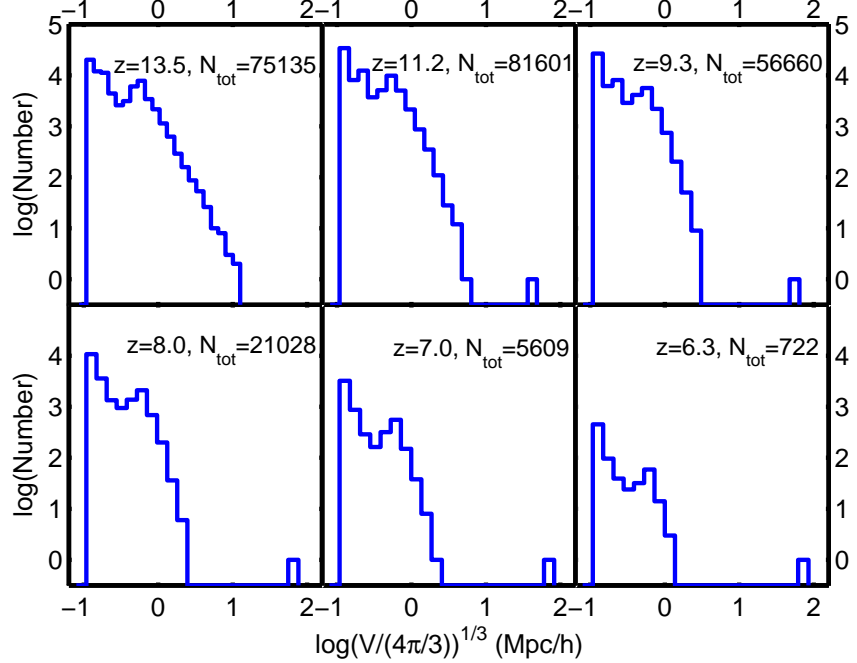


Fig. 2.— Number distributions of x_i -bubble volumes at redshifts $z = 13.5, 11.2, 9.3, 8.0, 7.0$, and 6.3 , respectively.

3. The Equivalent Width as a Probe of Reionization

The uniformly distributed IGM would produce only uniform absorption on the radio spectrum, it is the variation of density, ionization state, and spin temperature which produces varied absorption that is observable. This is illustrated in Fig. 3. One may define an *absorber* or a *leaker* as a continuous part of the spectrum for which

$$|\tau_\nu - \tau_0| > \tau_{th} \quad (2)$$

where τ_0 is the average optical depth over the whole simulation box at that redshift, τ_{th} is the threshold value. The strength of 21 cm absorption is typically not very strong due to its weak transition coefficient. We take $\tau_{th} = 0.002$, which could induce features observable with high signal to noise observation. The criteria $\tau_\nu - \tau_0 > \tau_{th}$ picks up absolute absorbers while the criteria $\tau_0 - \tau_\nu > \tau_{th}$ picks up absolute leakers. Alternatively, one can also use a relative definition

$$\frac{|\tau_\nu - \tau_0|}{\tau_0} > R \quad (3)$$

where R is the threshold, and is taken as 0.5 here. We will see later (in Fig. 7) that the morphology and distribution of the optically thin or thick regions remain nearly the same if we use a different

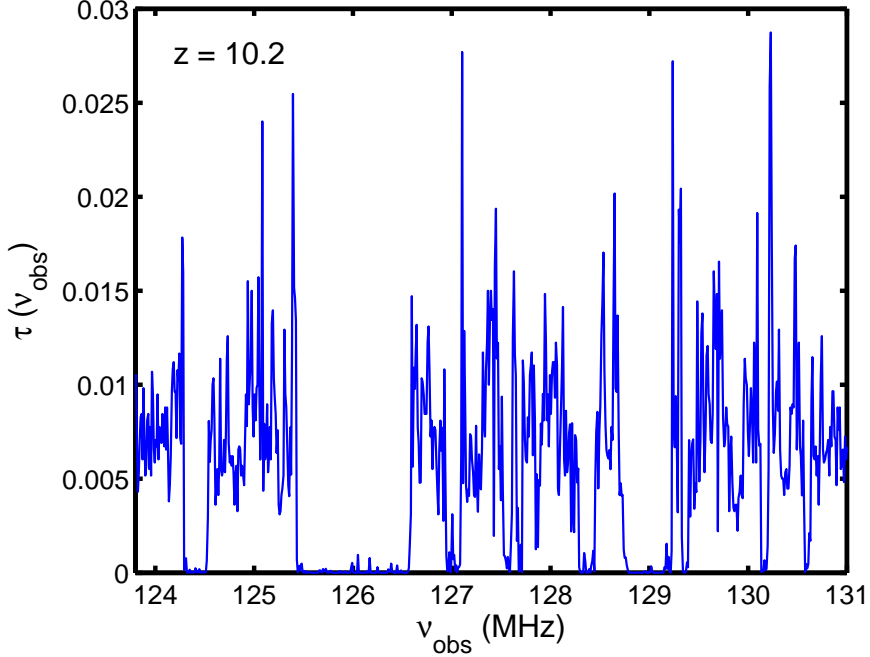


Fig. 3.— The optical depth as a function of observed frequency along a line of sight passing through the simulation box. The redshift here is 10.2.

threshold. In this way, one can select *relative absorbers* and *leakers*.

To characterize the strength of signals, we consider the equivalent width (EW) of both absorbers or leakers. For absolute or relative absorbers,

$$\begin{aligned}
 W_\nu &= \int_{\text{absorber}} \frac{|f_\nu - f_{IGM}|}{f_{IGM}} d\nu, \\
 &= \int_{\text{absorber}} (1 - e^{\tau_0 - \tau_\nu}) d\nu
 \end{aligned} \tag{4}$$

where f_{IGM} is the residual flux of a high redshift radio source after the mean absorption by the IGM, and f_ν is the flux at frequency ν . For absolute or relative leakers,

$$W_\nu = \int_{\text{leaker}} (e^{\tau_0 - \tau_\nu} - 1) d\nu. \tag{5}$$

Clearly ionized regions will produce leakers and neutral clumps will produce absorbers on high redshift quasar spectra.

Before using the equivalent width as our statistics, we test whether it is a good tracer of the ionized (neutral) regions, and to what extent we can extract x_i , ρ , and T_{IGM} information from EW

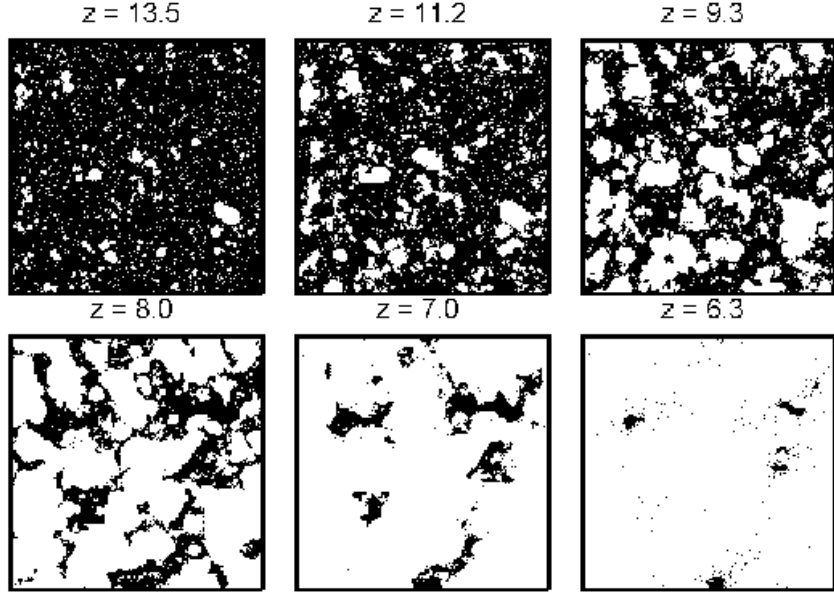


Fig. 4.— Distributions of relative optical depth at redshifts $z \sim 13.5, 11.2, 9.3, 8.0, 7.0$, and 6.3 . Regions with $(\tau_0 - \tau_\nu)/\tau_0 > 0.5$ (optically thin) are represented by white while other regions are shown as black. These are plots of slices in the simulation box with each side of $100 \text{ Mpc}/h$. The global ionization fractions are same as Fig. 1. The corresponding average optical depth for these redshifts are $\tau_0 = 1.1 \times 10^{-2}, 7.5 \times 10^{-3}, 4.4 \times 10^{-3}, 1.8 \times 10^{-3}, 4.8 \times 10^{-4}$, and 6.7×10^{-5} respectively.

statistics. This test includes two parts: (1) the consistency between ionized regions and optically thin regions, and (2) the correspondence between 3D bubbles and the projected 1D absorbers.

To do the first test, we display slices of optical depth field in Fig. 4. In the optical depth calculation, the spin temperature T_s is taken to be the temperature output from the simulation data. We have used the relative definition $(\tau_0 - \tau)/\tau_0 > 0.5$ to define the optically thin cells. Optically thin regions are shown as white while optically thick regions are shown as black. We see good agreement between optically thin regions in Fig. 4 and those highly ionized regions in Fig. 1, and the configurations match very well between the x_i -slices and τ -slices. For more quantitative comparison, we also made scatter plots of the absolute optical depth τ and the relative optical depth $(\tau_0 - \tau)/\tau_0$ versus ionized fraction x_i on a cell-by-cell basis in Fig. 5 (for $z = 9.3$). There is a strong correlation between the optical depth and the ionized fraction. Note that cells with high optical depth (large $\lg(\tau)$ or very negative $(\tau_0 - \tau)/\tau_0$) have low ionization fraction x_i , while high threshold on $(\tau_0 - \tau)/\tau_0$ picks out mostly highly ionized regions.

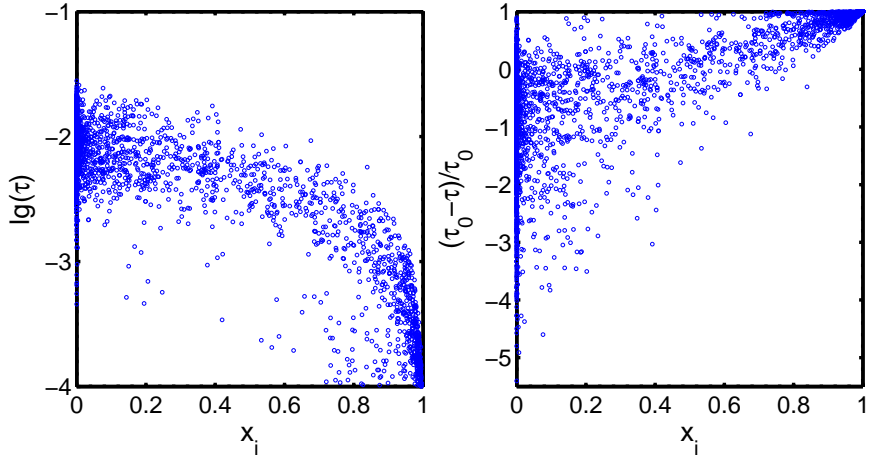


Fig. 5.— Scatter plots of 21 cm optical depth τ versus ionized fraction x_i (*left panel*) and the relative optical depth $(\tau_0 - \tau)/\tau_0$ versus ionized fraction x_i (*right panel*). The redshift shown here is $z = 9.3$.

We may also use the FoF algorithm to select and connect cells by the value of the optical depth instead of the ionization fraction. Size distributions of the optically thin bubbles (denoted as relative τ -bubbles) are shown in Fig. 6 for several redshifts. The size distribution of these relative τ -bubbles are apparently very similar to that of the x_i -bubbles, but the peaks are more smoothed, probably due to the mixture of ionization state and density information in optical depth. So the optical depth in the relative definition is a reasonable representative of the ionization status of the IGM. Although it smears out the characteristic scales of ionized bubbles, the τ -field does follow the large scale structure of the ionization field.

We also tried different relative thresholds in selecting these τ -bubbles, in order to see how the signals would change with the thresholds we used. Fig. 7 shows the optical depth slices at redshift 9.3 for thresholds $(\tau_0 - \tau)/\tau_0 > 0.1, 0.3, 0.7$, and 0.9 , respectively. The shapes and distributions of the bubbles are quite similar among these slices with different relative optical depth thresholds. The τ -slices with more strict thresholds have more dark dots (optically thicker regions) inside bubbles, and have less white dots (optically thinner regions) outside bubbles. All these τ -bubbles match well with x_i -bubbles, and similar results can be found for other redshifts. So the observational features in 21 cm forests would not change significantly if different threshold is adopted.

Features picked up with absolute threshold are more relevant to real observations. HII Bubbles and HI islands selected by the absolute threshold $|\tau_\nu - \tau_0| > 0.002$ for the corresponding 6 redshifts are shown in Fig. 8. Using this absolute optical depth threshold, there are both bubbles and islands at three higher redshifts (i.e. 13.5, 11.2, and 9.3), which generate leakers and absorbers on spectra

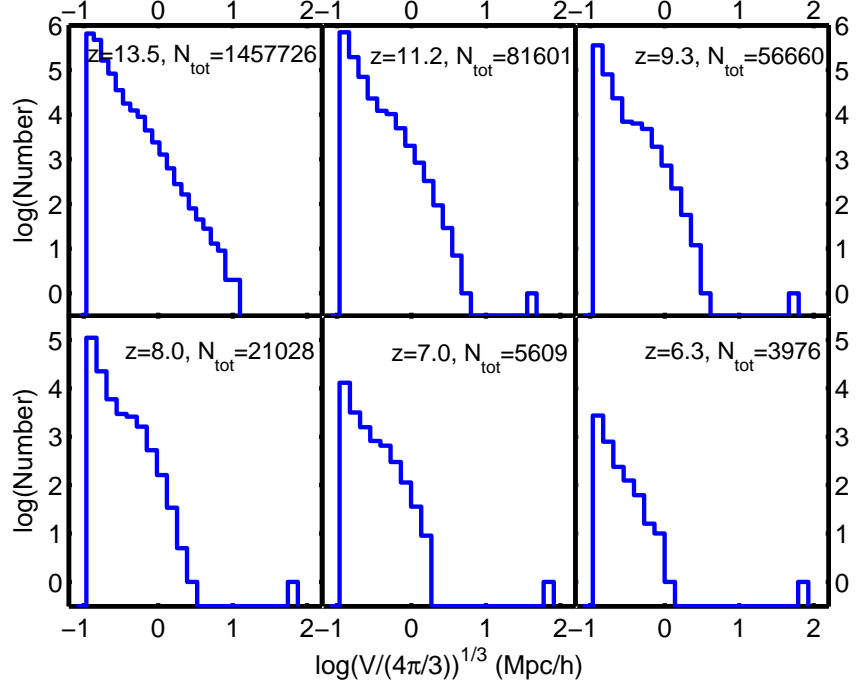


Fig. 6.— Number distributions of relative τ -bubble volumes at redshifts $z = 13.5, 11.2, 9.3, 8.0, 7.0$, and 6.3 , respectively. The criteria to select these bubbles is $(\tau_0 - \tau_\nu)/\tau_0 > 0.5$.

respectively. At lower redshifts there are only islands, since the average optical depth itself is smaller than 0.002 (i.e. at redshifts 8.0, 7.0, and 6.3 here), so we could only observe absorbers. For the leakers, smaller threshold must be used in order to find them at these redshifts. The shapes and distributions of these τ -bubbles are similar to those selected by relative thresholds. Combined with Fig. 1 and Fig. 4, we come to the conclusion that no matter relative or absolute threshold we use, the optical thin regions follow the highly ionized region very well, at least on large scales. Size distributions of absolute τ -bubbles and τ -islands for the three higher redshifts and those of absolute τ -islands for the other three lower redshifts are shown in Fig. 9.

In order to see whether the optical depth (hence the EW statistics) is a good tracer of density fluctuations, we plot density slices in Fig. 10. But because of the limited resolution of the simulation (the overdensity is smoothed within each cell), the density contrast is very small (typically $\delta < 1$) on these scales, and do not show much evolution, and there is little correlation with the ionization fraction. This means that we would miss strong absorbers produced by small but highly dense regions such as cosmic webs, this would affect the accuracy of this simulation in representing the real case.

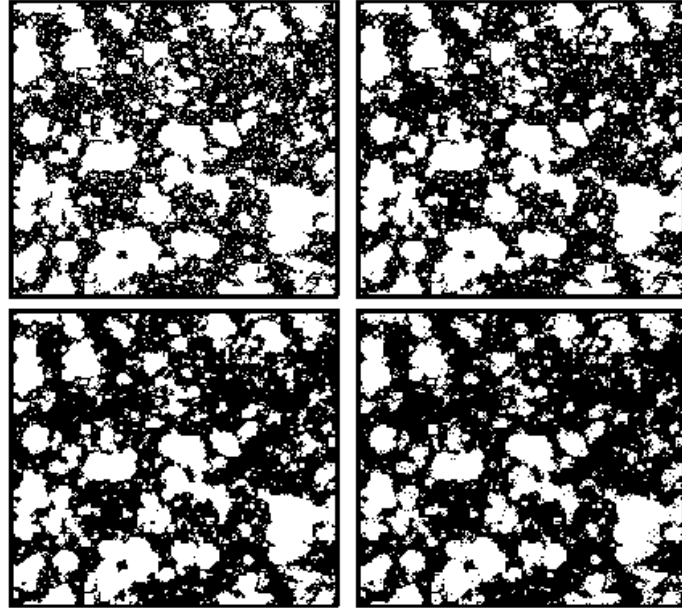


Fig. 7.— Distributions of optical depth at redshift $z = 9.3$, when the average optical depth $\tau_0 = 4.4 \times 10^{-3}$. Regions with relative optical depth $(\tau_0 - \tau_\nu)/\tau_0 >$ threshold (optically thin) are represented by white while other regions are shown as black. The relative thresholds are 0.1, 0.3, 0.7, and 0.9 from left to right and top to bottom, respectively. These are plots of slices in the simulation box with each side of 100 Mpc/h.

Can we get some information about the temperature of the IGM from 21 cm forest signals? Although there is no heating information incorporated in the simulation, and the gas temperature is derived from the velocity dispersion of the particles, it is still possible to test the sensitivity of optical depth and the forest signal to the IGM temperature, by assuming several different gas temperatures. In top panels of Fig. 11, we plot relative τ -slices at redshift 9.3 for the IGM temperatures of 10^1 K, the gas temperature from simulation, and 10^2 K, from left to right, respectively (in this excise we set the same temperature at every point within the simulation volume). Absolute τ -slices with the corresponding gas temperatures are plotted in bottom panels of Fig. 11.

Obviously, τ -slices with relative thresholds are insensitive to the gas temperature, while the absolute τ -slices are very sensitive. When we raise the IGM temperature to be 10^2 K, the average optical depth at redshift 9.3 falls below the threshold 0.002, and no optical depth could drop below the mean value by 0.002, so there is no optically thin region in the absolute definition in this redshift, just as the three slices of lower redshifts in Fig. 8. If we raise the IGM temperature further to be 10^3 K, then very few regions could have optical depth larger than the average depth

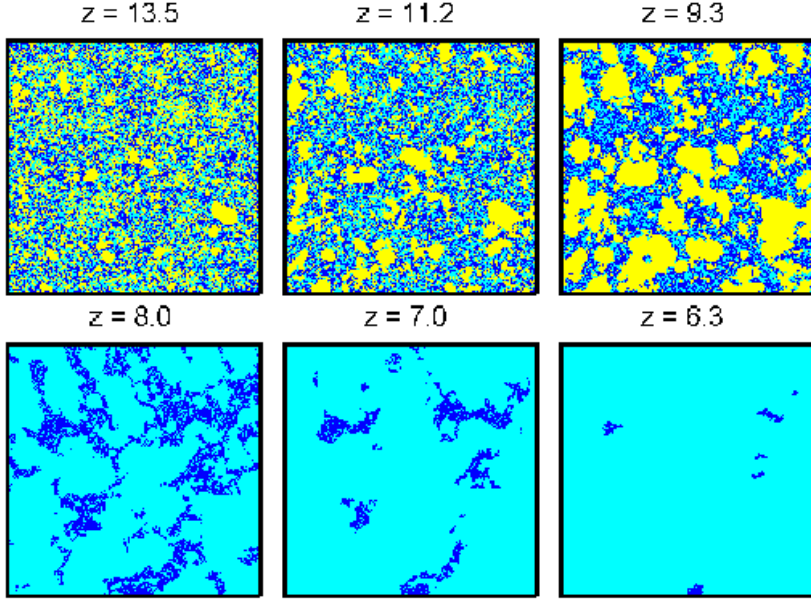


Fig. 8.— Distributions of absolute optical depth at six redshifts: $z = 13.5$, $z = 11.2$, $z = 9.3$, $z = 8.0$, $z = 7.0$, and $z = 6.3$. Regions with $\tau_0 - \tau_\nu > 0.002$ (optically thin) are represented by yellow, regions with $\tau_\nu - \tau_0 > 0.002$ (optically thick) are shown as dark blue, and the other regions lie in between are shown as light blue. The corresponding average optical depth for these redshifts are $\tau_0 = 1.1 \times 10^{-2}$, 7.5×10^{-3} , 4.4×10^{-3} , 1.8×10^{-3} , 4.8×10^{-4} , and 6.7×10^{-5} respectively. These are plots of slices in the simulation box with each side of 100 Mpc/h.

by 0.002. Hence, we could easily extract T_K information from absolute τ threshold observations while ionization state of the IGM could be extracted from relative τ threshold observations.

It is very interesting to find a method to measure the IGM temperature during the epoch of reionization. While the kinetic temperature of the IGM and spin temperature of hydrogen are usually assumed to be much higher than the CMB temperature in 21 cm power spectrum analysis, and the T_K information of the IGM is totally erased in “21 cm tomography” observations, the “21 cm forest” observations serve as an excellent tool to separate the T_K information from the density and ionization status.

Now we have seen some correspondence between the optical depth and the ionized fraction selected bubbles. However, in order to guarantee the validity of our EW statistics, we should also test the correspondence between observed absorbers and τ -islands, or leakers and τ -bubbles. To do so, we put random lines of sight through the simulation box, calculated the EW of each absolute absorber, and recorded their center positions. Then we checked whether the centers of absorbers

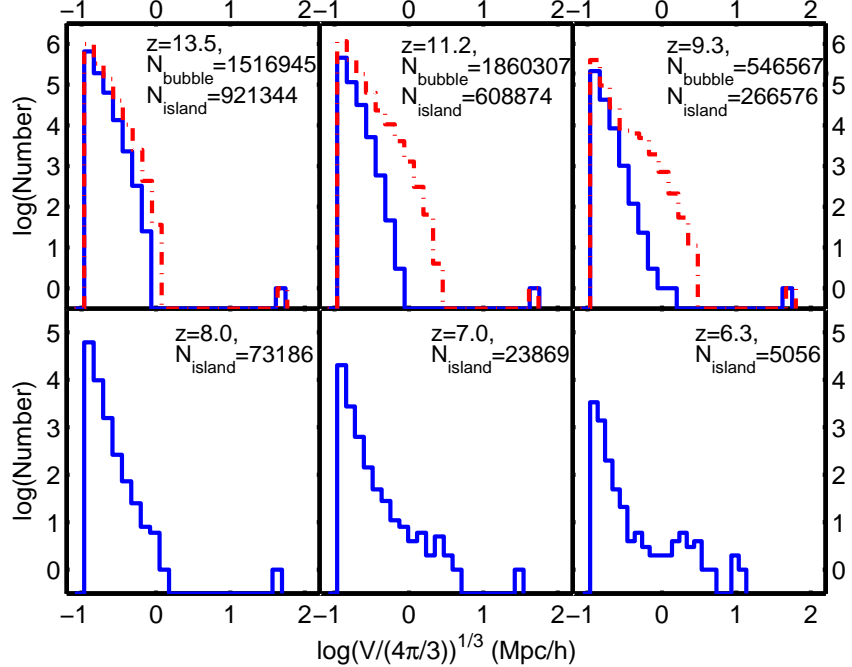


Fig. 9.— Size distributions of absolute τ -islands at redshifts $z = 13.5, 11.2, 9.3, 8.0, 7.0$, and 6.3 , respectively (blue solid lines), and those of absolute τ -bubbles at the three higher redshifts $z = 13.5, 11.2$, and 9.3 (red dot-dashed lines). The criteria to select these islands is $\tau_\nu - \tau_0 > 0.002$, and the criteria for these bubbles is $\tau_0 - \tau_\nu > 0.002$.

reside in those τ -islands we found. Results show that most EW features have their centers within τ -islands, and those EW features which are not in τ -islands are in one-cell-islands, which were not defined as islands in our “FOF” algorithm. Fig. 12 shows scatter plots of absorbers’ equivalent width and the volumes of their corresponding τ -islands in which the centers of these absorb features reside. Absolute definition is used here for absorbers and islands, as is relevant in real observations. Although there is some correlation between the volume and equivalent width, we see that the scatter is very large, as the line of sight may pass through the region far from the center. One can also see a spike in the volume distribution, which corresponds to the connected HI region (partially ionized at lower redshifts) in the simulation box. This connected island does not disappear until the overall optical depth drops as seen at $z = 7.0$ when some places in the island failed to connect those regions around them and give birth to many small islands. More clearly, at $z = 6.3$, one connected island fragmented into three big islands and many smaller ones. They exist till late stages of reionization because of the self-shielding effect of these dense regions.

In summary, optical depth can be a reasonable tracer of the ionized fraction and the equivalent

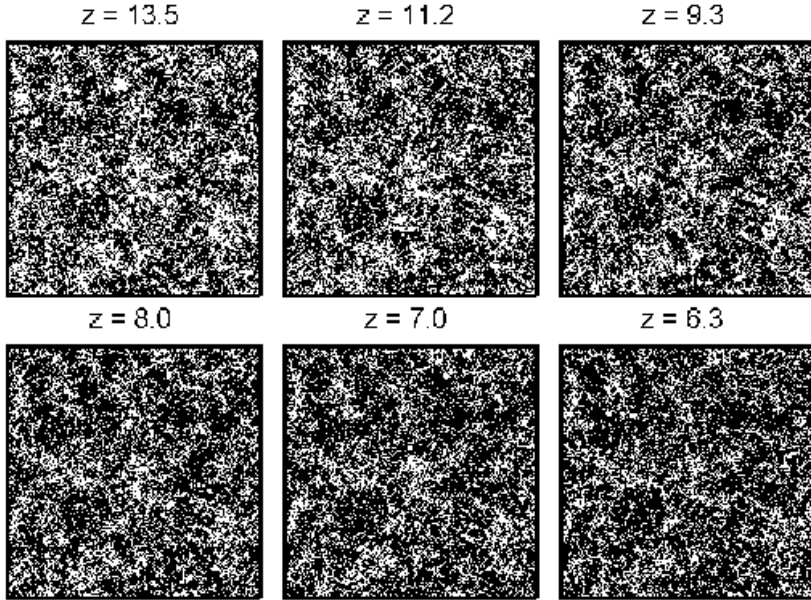


Fig. 10.— Distributions of overdensity at different redshifts. Overdense regions are represented by white while underdense regions are shown as black.

width could serve as a great probe of cosmic reionization. While the features picked with relative thresholds are better in extracting ionization information, the features picked by absolute thresholds are very sensitive to the IGM temperature. However, the small scale density fluctuation is not incorporated in our simulation, and the density field on large scales plays a minor role in determining the optical depth. So we do not expect to get information about local density fluctuation from EW statistics. In addition, we see correspondence between the 3-dimensional bubbles and the projected 21 cm forest signals.

4. Statistical Distribution of 21 cm Forest Signals

First we calculate the average optical depth τ_0 over the whole simulation box for each redshift z , and take this τ_0 as the optical depth of the intergalactic medium, τ_{IGM} . Then we put 400 random lines of sights (LOS) through each side of the simulation box at a specific redshift z , and calculate the optical depths along each line of sight as a function of observed frequency. Using the threshold $(\tau_\nu - \tau_0) > 0.002$, we pick every absorber along each line of sight, then calculate and record the EWs of them for every random LOS. The periodic boundary condition is employed here.

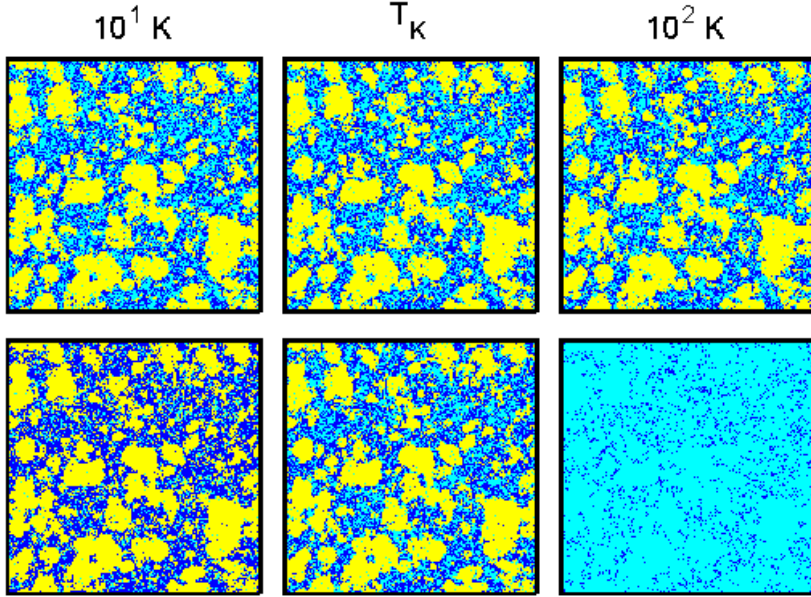


Fig. 11.— Distributions of optical depth with different gas temperatures at redshift $z = 9.3$. Top panels: optically thin regions with *relative threshold* $(\tau_0 - \tau_\nu)/\tau_0 \geq 0.5$ are shown as yellow, optically thick regions with $(\tau_\nu - \tau_0)/\tau_0 \geq 0.5$ are shown as dark blue, while other regions in between are labeled as light blue. The gas temperatures are assumed to be 10^1 K, gas temperature based on velocity dispersion, and 10^2 K, from left to right, respectively. Bottom panels: regions with *absolute threshold* $\tau_0 - \tau_\nu > 0.002$ are shown as yellow, regions with $\tau_\nu - \tau_0 > 0.002$ are shown as dark blue, while other regions are shown as light blue. The temperatures are the same as top panels.

The number densities of absorbers and leakers are shown in Fig. 13. The total number of these absorbers decreases significantly with decreasing redshift throughout the reionization. This is especially obvious for absorbers of small equivalent width, since the small islands were being ionized and becoming parts of ionized bubbles as the reionization proceeded. However, the number of absorbers with the largest equivalent width does not change as much, and the largest absorbers seem to persist to lowest redshifts. This is due to the self-shielding effect of the dense neutral regions, which precisely generated the spikes seen in Fig. 12. They give us an opportunity to observe large absorbers even at lower redshifts. For the leakers, the number of smaller ones decreases with decreasing redshift since those small ionized bubbles were merging to generate larger ones, while the number density of larger leakers increases.

Besides the equivalent width, the width of these absorbers or leakers is also an observable in radio probes, and it has good correspondence to the equivalent width as shown in Fig. 14. Just

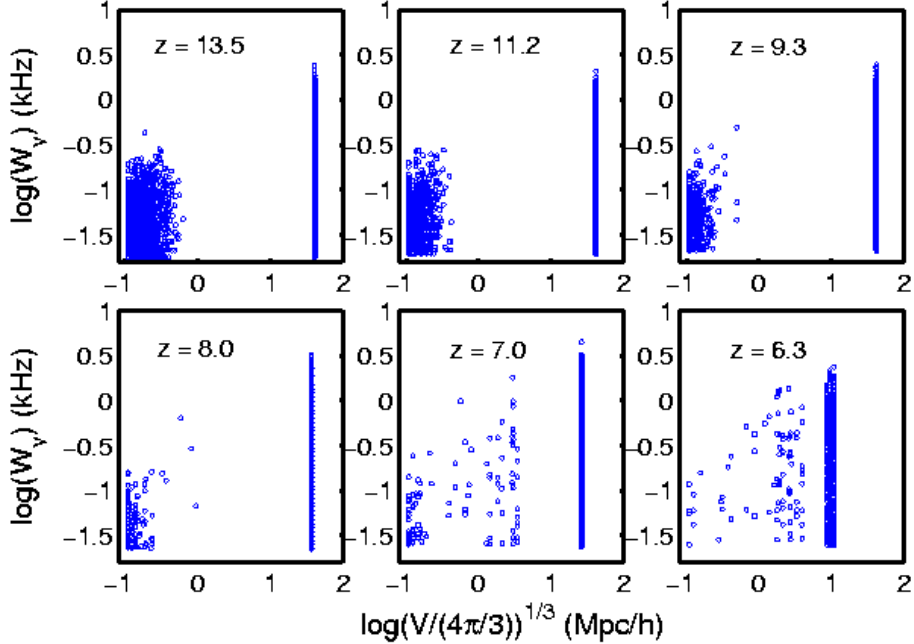


Fig. 12.— Scatter plots of volumes of τ -islands which hold absorbers versus EW of those absorbers at different redshifts.

as EWs of absorbers and their corresponding τ -islands were shown in Fig. 12, Fig. 14 shows the consistency between feature widths and the τ -islands or τ -bubbles associated with them. The maximum width of an absorber created by each island has a stronger correlation with the island size, and the same applies to relation between bubble size and the maximum width of leakers.

The optical depth is very sensitive to the IGM temperature. We calculated the number density of absolute leakers that have $W_\nu > 1$ kHz as a function of the gas temperature. The results for several redshifts are presented in Fig. 15. The number densities of potentially observable absorbers decrease rapidly as the temperature increases. This means, on one hand, with the first generation of low frequency equipments, we may not be able to observe the signals that we are looking for if the IGM was really heated up, but on the other hand, we could obtain information on the gas temperature at the epoch of reionization from 21 cm forest observations. This is important because the IGM temperature contains very rich information about early structure formation, including the initial mass function of the first stars, properties of early mini-quasars and related X-ray heating, etc. In this sense, the 21 cm forest can be a powerful tool not only to probe the IGM in the early universe, but also to give constraints on the properties of early structures.

Our prediction of the mean IGM optical depth is a little smaller than those by Carilli et al. (2002) at higher redshifts but larger than theirs at lower redshifts. For example, at $z = 12$

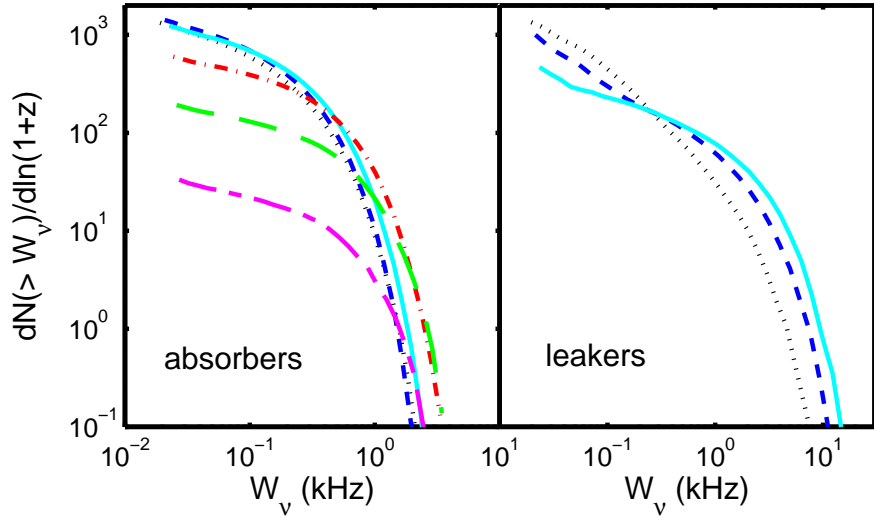


Fig. 13.— The number density of absolute absorbers (left panel) and leakers (right panel) with equivalent width larger than W_ν , as a function of W_ν . The curves for redshifts 13.5, 11.2, 9.3, 8.0, 7.0, and 6.3 are represented by dotted (black) line, short-dashed (blue) line, solid (cyan) line, dot-dashed (red) line, long-dashed line (green), and long-and-short-dashed (purple) line respectively for absorbers, and only the three curves for higher redshifts are shown for leakers with the same line types as those for absorbers at the same redshifts.

Carilli et al. (2002) found that $\tau_{IGM} \sim 1\%$, and some of the high-density regions reach $\tau \sim 5\%$ and above; by $z \sim 8$, the mean IGM optical depth has dropped to $\tau_{IGM} \sim 0.1\%$. In our simulation, however, $\tau_{IGM} \sim 0.9\%$ at $z \sim 12$ and it only drops to $\tau_{IGM} \sim 0.18\%$ at $z = 8$.

However, unlike Carilli et al. (2002), we find very few strong absorbers. In our simulation box, only about one in two million cells would have $\tau \geq 5\%$ at $z \sim 12$, and no absorbers has $\tau \geq 2\%$ at $z \leq 10$, while Carilli et al. (2002) still predicted 50 lines per unit redshift with $\tau \geq 2\%$ at $z = 10$ and about 4 lines per unit redshift at $z = 8$. Some of these differences may be due to the different values of cosmological parameters adopted in the two simulation. However, the main difference probably comes from the different box size of the simulations. Carilli et al. (2002) used a simulation with smaller volume but higher spatial resolution (Gnedin 2000), in which the typical values of the cosmic overdensity $\delta \sim 10$. Our simulation has a much larger box volume, which is much more reliable for large scale reionization, but the size of each cell is larger. This affects the density fluctuation dramatically, and our typical overdensity within each cell is $\delta < 1$, with a few

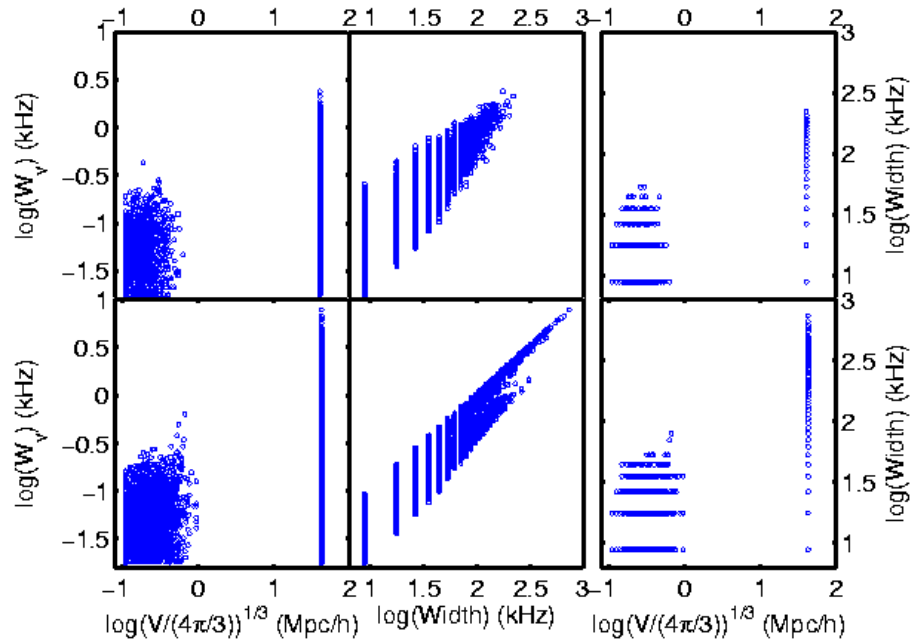


Fig. 14.— Top panels: the correspondence among the absorbers' width, their equivalent width, and the volumes of τ -islands which created them. Bottom panels: the correspondence among the leakers' width, their equivalent width, and the volumes of τ -bubbles which created them. The redshift shown here is 13.5.

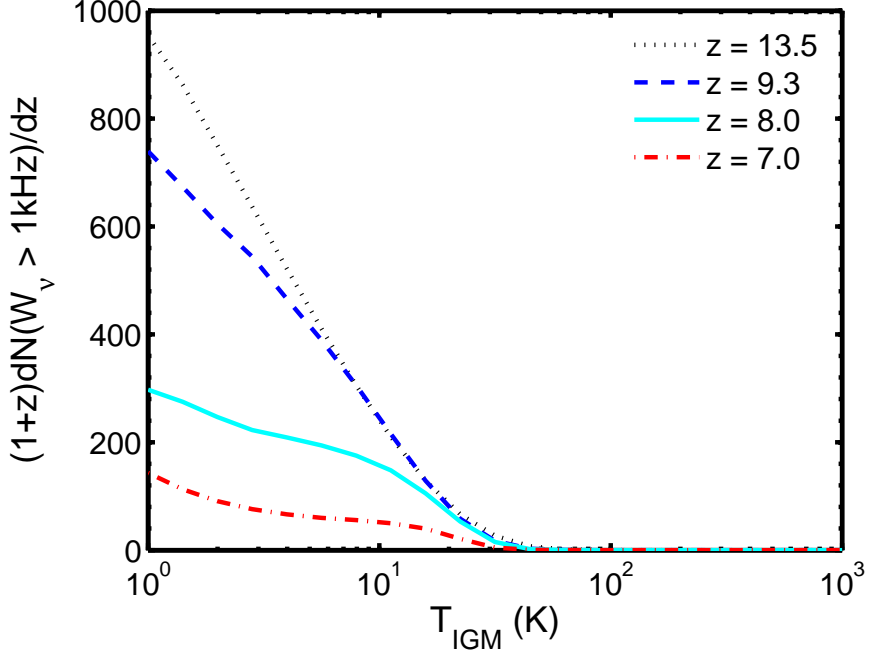


Fig. 15.— Number density of absolute absorbers with equivalent width $W_\nu > 1$ kHz as a function of the IGM temperature. The redshifts are $z = 13.5$ (dotted, black), $z = 9.3$ (dashed, blue), $z = 8.0$ (solid, cyan), and $z = 7.0$ (dot-dashed, red), respectively.

regions have $\delta > 1$. As seen in Fig. 10, the density field evolves very little when smoothed within the cells, though at smaller scales there must be some evolution in density contrast. Therefore, the resultant local optical depth is underestimated.

On the other hand, the first HII regions start to appear at redshift about 8 in the simulation by Gnedin (2000), which is much later than that in our simulation (Shin, Trac & Cen 2008). As a result, Carilli et al. (2002) found higher optical depth of 21 cm forest than us at high redshift. Further, in Carilli et al. (2002), those absorbers are typically filaments. They are at first shock-heated to about 100 K, and at $z < 10$ Ly α heating increases the mean spin temperature to above 100 K. In our simulation, the resolution is not high enough to capture the filaments anyway. The Ly α heating is also unlikely to heat the gas to so high a temperature, more likely it could only heat up the IGM to a temperature below 100 K before reionization (Chen & Miralda-Escudé 2004; Yue et al. 2009). In the simulation, these heating mechanisms are not incorporated, and the temperature is just from the velocity dispersion of the particles. Therefore we have lower spin temperature and this results in the higher mean IGM optical depth at lower redshifts, though we can artificially adjust the gas temperature as a proxy for incorporating the various heating mechanisms.

5. The number of high redshift radio sources

To observe the absorption or leak features in the spectrum, the spectrum of the point source has to be observed with a certain precision, which depends on the brightness of the quasar. The minimum detectable flux density of an interferometer is related to the system temperature T_{sys} , the effective aperture area A_{eff} , channel width $\Delta\nu_{\text{ch}}$, integration time t , and the signal-to-noise ratio S/N by:

$$\Delta S_{\text{min}} = \frac{2 k_{\text{B}} T_{\text{sys}}}{A_{\text{eff}} \sqrt{\Delta\nu_{\text{ch}} t}} \frac{S}{N}. \quad (6)$$

For the observation of resolved signals (i.e. the resolution pixel $\Delta\nu_{\text{ch}}$ is narrower than the width of the feature to be observed), the lower limit of the flux density of background sources for an observation of absorbers or leakers with $|\tau_{\nu} - \tau_0| \geq \tau_{th}$ (when the τ_{ν} , τ_0 , and τ_{th} are all very small) is:

$$\begin{aligned} S_{\text{min}} = & 181.8 \text{mJy} \left(\frac{S/N}{5} \right) \left(\frac{0.002}{\tau_{th}} \right) \left(\frac{1 \text{kHz}}{\Delta\nu_{\text{ch}}} \right)^{1/2} \\ & \times \left(\frac{2 \times 10^3 \text{m}^2 \text{K}^{-1}}{A_{\text{eff}}/T_{\text{sys}}} \right) \left(\frac{100 \text{hr}}{t} \right)^{1/2}. \end{aligned} \quad (7)$$

where the ratio $A_{\text{eff}}/T_{\text{sys}}$ is an intrinsic parameter describing the sensitivity of an interferometry array. The systematic temperature is the sum of the receiver noise and the temperature of the uncleaned foregrounds.

However, the optical depths of the “absorbers” and “leakers” are small, while the signals are relatively wide($10^1 \sim 10^2$ kHz), so that observation of unresolved signals (or just below resolution) is more promising. In this case, the lower limit of the flux density for an observation of absorbers or leakers with $W_{\nu} \geq W_{th}$ is:

$$\begin{aligned} S_{\text{min}} = & 11.5 \text{mJy} \left(\frac{S/N}{5} \right) \left(\frac{1 \text{kHz}}{W_{th}} \right) \left(\frac{\Delta\nu_{\text{ch}}}{1 \text{MHz}} \right)^{1/2} \\ & \times \left(\frac{2 \times 10^3 \text{m}^2 \text{K}^{-1}}{A_{\text{eff}}/T_{\text{sys}}} \right) \left(\frac{100 \text{hr}}{t} \right)^{1/2}. \end{aligned} \quad (8)$$

The demanded flux density of the background source is much lower compared to the resolved observations, making more high redshift radio sources qualified for such observations.

We now investigate how many such quasars can be observed. Specifically, we calculate the number of quasars with flux density at the observed frequency $\nu = 1420.4/(1+z)$ MHz larger than the lower limit described above. In the following, we assume that all the radio quasars are of the same spectral energy distribution with that of the powerful radio galaxy Cygnus A, i.e. $P_{\nu} \propto \nu^{-1.05}$ (Carilli et al. 2002). Then the limiting flux density converts to a limiting luminosity density at a rest-frame frequency of 151 MHz, P_{151}^{min} .

Jarvis et al. (2001) have pointed out that at $z = 4$, the comoving number density of radio sources with luminosity density at the frequency 151 MHz, $P_{151} \geq 6 \times 10^{35} \text{ergs s}^{-1} \text{Hz}^{-1}$, is $2.4 \times$

10^{-9} Mpc^{-3} . We extrapolate this number density to higher redshift and lower luminosity. Assuming that the comoving number density of qualified quasars at redshift z is given by $n_{\text{CM}}(P_{151} \geq P_{151}^{\min}, z)$, and according to the best-fitting luminosity function given by Jarvis et al. (2001), we have

$$dn_{\text{CM}}(P_{151}, z)/dP_{151} = C(z) P_{151}^{-2.2}. \quad (9)$$

where $C(z)$ is a normalization constant, which in general is a function of redshift. But it is suggested by Jarvis et al. (2001) that there is very little evidence for an abrupt decline in the comoving space density of the most luminous low-frequency-selected sources at high redshift, and the best-fitting model gives a constant comoving space density. If, optimistically, we hypothesize quasars evolve according to the flat model, i.e. the number density does not vary with redshift in the comoving coordinate, then the number of qualified quasars ($P_{151} \geq P_{151}^{\min}$) in the whole sky per redshift interval is:

$$\frac{dN}{dz} = \frac{C}{1.2} P_{151}^{\min-1.2} \times 4\pi r_{\text{CM}}^2(z) \frac{dr_{\text{CM}}(z)}{dz}, \quad (10)$$

where $r_{\text{CM}}(z) = \int_0^z c dz/H(z)$ is the comoving coordinate corresponding to redshift z . On the other hand, based on optically selected quasars from SDSS, Cirasuolo et al. (2006) suggest that independent of the adopted radio spectral index, the drop in the space density of optically bright radio loud quasars between $z \sim 2$ and $z \sim 4.4$ is at most a factor $\sim 1.5 - 2$. If we adopt the upmost factor 2, then

$$C(z) = C(z=4) \exp[-\frac{\ln 2}{2.4} (z-4)]. \quad (11)$$

We plot the number of quasars which satisfy the above criteria for probing signals with $W_\nu \geq 1 \text{ kHz}$ in Fig. 16 for the flat evolution case in the left panel, and for the evolved case in the right panel. Here we choose three values of sensitivity, $A_{\text{eff}}/T_{\text{sys}} = 5000 \text{ m}^2 \text{K}^{-1}$, $2000 \text{ m}^2 \text{K}^{-1}$, and $1000 \text{ m}^2 \text{K}^{-1}$ respectively, which can be achieved in future observation programs. The Square Kilometer Array (SKA) will have $A_{\text{eff}}/T_{\text{sys}} = 5000 \text{ m}^2 \text{K}^{-1}$ at the frequency between 70 MHz and 300 MHz (see <http://www.skatelescope.org/>), and the Low Frequency Array (LOFAR) could marginally achieve $A_{\text{eff}}/T_{\text{sys}} = 1000 \text{ m}^2 \text{K}^{-1}$ at 200 MHz (<http://www.lofar.org/>). We can see that for the flatly evolved quasar density, there would be many bright quasars which could be used as our background sources. However, for the steeply evolved quasar model, those suitable background quasars would be very few.

6. Conclusions

We used a numerical simulation with star formation and radiative transfer (Shin, Trac & Cen 2008) to study the 21 cm forest signals during the epoch of reionization. We first defined absolute and relative absorbers and leakers on spectra of background sources produced by structures along the line of sight, and checked whether the absorbers or leakers can represent the ionization and thermal state of the IGM. We found that the optical depth can be a reasonable tracer of the ionized

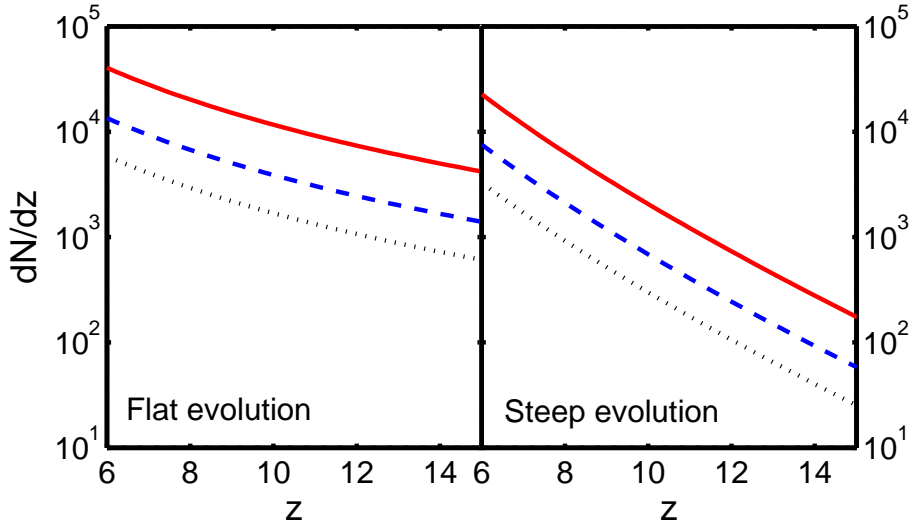


Fig. 16.— The number of quasars in the whole sky that can be used to detect signals with $W_\nu \geq 1\text{kHz}$ per redshift interval. *Left panel*: the number of qualified quasars in the flat evolution model. *Right panel*: the number in the steep evolution model. The sensitivity of the radio array is taken to be $A_{\text{eff}}/T_{\text{sys}} = 5000 \text{ m}^2\text{K}^{-1}$, $2000 \text{ m}^2\text{K}^{-1}$, and $1000 \text{ m}^2\text{K}^{-1}$ for the *red-solid*, *blue-dashed*, and *black dotted* line, respectively. The integration time is assumed to be 100 hours here.

fraction of the IGM, and the equivalent width could serve as a great probe of cosmic reionization. The features selected by absolute threshold in optical depth are also very sensitive to the IGM temperature, so the temperature information of the IGM could be separated from the ionization fraction and density fluctuations with 21 cm forest observation, making it a good complement to 21 cm tomography observation. At the scales we studied, the density fluctuation plays a minor role in determining the optical depth. Also, we see correspondence between the 3-dimensional bubbles and the projected 21 cm forest signals.

The number densities of leakers and absorbers with different equivalent widths evolve with redshift, showing the evolution of ionization status of the IGM. While the total number of absorbers decreases significantly with decreasing redshift, the largest absorbers persist to low redshifts because of the self-shielding effect. As for the leakers, diminished small ones and ballooning large ones with time show the signature of merging ionized bubbles. From the largest width of leakers or absorbers in 21 cm forest spectra, we may infer the size of ionized bubbles or neutral islands at specific redshifts.

The most important advantage regarding the 21 cm forest observation is its sensitive dependence of signals on the IGM temperature. The number density of potentially observable signals decreases dramatically with the increasing gas temperature, so the temperature of the IGM at each redshift could be constrained potentially through the 21 cm forest observations. As the thermal history of the IGM carries rich information about the first luminous sources, including the population of the first stars, properties of mini-quasars, and complex heating processes, the 21 cm forest observation is a potentially powerful probe of the early structure formation of the universe. The measurement of the gas temperature would also help improve the precision of the measurement of cosmological parameters.

We also compared our results with a previous work by Carilli et al. (2002), who used a simulation with higher resolution but smaller volume (Gnedin 2000). While our simulation has a much larger volume which is necessary to account for large HII regions at late epochs of reionization, small-scale structures such as small filaments and minihalos are not resolved, especially in the binned data used for post-analysis. With higher resolution simulations, higher gas overdensities and hence higher optical depths would be expected. Since heating processes are not included in our simulation, the assumed gas temperature is not realistic, but we do consider a range of possible temperatures. With these limitations, we can not make an accurate prediction for the signal, but instead provide a basic expected range. Nonetheless, our simulation does reveal some qualitative features of the large scale 21cm signal, and propose here that the 21 cm forest observations, especially the EW statistics, could play an important role in extracting temperature information of the IGM. We reserve more realistic investigation of the 21 cm forest to future works, for example by using higher-resolution versions of the hydro+radiative transfer simulations presented in Trac, Cen & Loeb (2008), which have self-consistent hydrodynamics and temperature evolution.

Finally we discussed the the number of luminous high redshift radio sources which is potentially available for observing such forest signals. We investigated the requirement on the luminosity of background radio sources for the observation of signals with equivalent widths larger than 1kHz. We considered how the number of qualified quasars in the whole sky evolves with redshift according to two models. If quasars evolves according to the flat evolution model, we would have sufficient quasars as background sources at high redshift; if quasars evolve fast, however, only those signals at relatively lower redshift can be observed in the near future.

We thank Bin Yue, Andrea Ferrara, Steven Furlanetto and Chris Carilli for helpful discussion. This research is supported in part by the NSFC grant 10525314, 10503010, 10373001, 10773001, by the CAS grant KJCX3-SYW-N2, MoST 973 grant 2007CB815401, and by NASA ATP grant NNG06GI09G. Computing resources were in part provided by the NASA High-End Computing (HEC) Program through the NASA Advanced Supercomputing (NAS) Division at Ames Research Center.

REFERENCES

Barkana, R. & Loeb, A. 2005, *ApJ*, 624, L65

Becker R. H. et al. 2001, *AJ*, 122, 2850

Bolton, J. S. & Haehnelt, M. G. 2007a, *MNRAS*, 374, 493

Bolton, J. S. & Haehnelt, M. G. 2007b, *MNRAS*, 381, 35

Carilli, C. L., Gnedin, N. Y., & Owen, F. 2002, *ApJ*, 577, 22

Chen, X. & Miralda-Escudé, J., 2004, *ApJ* 602, 1

Choudhury, T. R. 2009, arXiv:0904.4596

Choudhury, T. R. & Ferrara, A. 2007, *MNRAS*, 380, L6

Ciardi, B. & Ferrara, A. 2005, *SSRv*, 116, 625 (updated in 2008: astrar-ph/0409018v2)

Ciardi, B., Stoehr, F., & White, S. D. M. 2003, *MNRAS*, 343, 1101

Cirasuolo, M., Magliocchetti, M., Gentile, G., Celotti, A., Cristiani, S., & Danese, L. 2006, *MNRAS*, 371, 695

Cohn, J. D. & Chang, T.-C. 2007, *MNRAS*, 374, 72

Dijkstra, M., Wyithe, J. S. B., & Haiman, Z. 2007, *MNRAS*, 379, 253

Dunkley J. et al. 2009, *ApJS*, 180, 306

Fan, X., Carilli, C., & Keating, B. 2006, *ARAA*, 44, 415

Field, G. B. 1959, *ApJ*, 129, 525

Furlanetto, S., 2006, *MNRAS*, 370, 1867.

Furlanetto, S. R. & Loeb, A. 2002, *ApJ*, 579, 1

Furlanetto, S. R. & Oh, S. P. 2005, *MNRAS*, 363, 1031

Furlanetto, S. R., Oh, S. P., & Briggs, F. H. 2006, *PhR*, 433, 181

Furlanetto, S. R., Sokasian, A., & Hernquist, L. 2004a, *MNRAS* 347, 187-195

Furlanetto, S. R., Zaldarriaga, M., & Hernquist, L. 2004b, *ApJ*, 613, 1

Furlanetto, S. R., Zaldarriaga, M., & Hernquist, L. 2004c, *ApJ*, 613, 16

Gallerani, S., Salvaterra, R., Ferrara, A., and Choudhury, T. R. 2008, *MNRAS*, 388, L84

Gnedin, N. Y. 2000, *ApJ*, 535, 530

Gunn J. E. & Peterson B. A. 1965, *ApJ*, 142, 1633

Haiman, Z., Abel, T., & Rees, M. J. 2000, *ApJ*, 534, 11

Haiman, Z. & Cen, R. 2005, *ApJ*, 623, 627

Hinshaw G. et al. 2009, *ApJS*, 180, 225

Iliev, I. T., Mellema, G., Pen, U.-L., Merz, H., Shapiro, P. R., & Alvarez, M. A. 2006, *MNRAS*, 369, 1625

Iliev, I. T., Mellema, G., Shapiro, P. R., & Pen, U.-L. 2007, *MNRAS*, 376, 534

Iliev, I. T., Shapiro, P. R., Ferrara, A., & Martel, H. 2002, *ApJ*, 572, L123

Ioka, K. & Mészáros, P. 2005, *ApJ*, 619, 684

Jarvis, M. J., Rawlings, S., Willott, C. J., Blundell, K. M., Eales, S., & Lacy, M. 2001, *MNRAS*, 327, 907

Kashikawa, N. et al. 2006, *ApJ*, 648, 7

Lidz, A., McQuinn, M., Zaldarriaga, M., Hernquist, L., & Dutta, S. 2007, *ApJ*, 670, 39

Madau, P., Meiksin, A., & Rees, M. J. 1997, *ApJ*, 475, 429

Malhotra, S. & Rhoads, J. E. 2004, *ApJ*, 617, L5

Malhotra, S. & Rhoads, J. E. 2006, *ApJ*, 647, L95

Maselli, A., Gallerani, S., Ferrara, A., & Choudhury, T. R. 2007, *MNRAS*, 376, L34

McQuinn, M., Hernquist, L., Zaldarriaga, M., & Dutta, S. 2007a, *MNRAS*, 381, 75

McQuinn, M., Lidz, A., Zaldarriaga, M., Hernquist, L., & Dutta, S. 2008, *MNRAS*, 388, 1101

Mellema G., Iliev I. T., Pen U. L., & Shapiro P. R. 2006, *MNRAS*, 372, 679

Mesinger, A. & Furlanetto, S. 2008a, *MNRAS*, 386, 1990

Mesinger, A. & Furlanetto, S. 2008b, *MNRAS*, 385, 1348

Mesinger, A. & Haiman, Z. 2004, *ApJ*, 611, L69

Mesinger, A. & Haiman, Z. 2007, *ApJ*, 660, 923

Mészáros, P. 2002, *ARA&A*, 40, 137

Miralda-Escudé, J. 1998, *ApJ*, 501, 15

Miralda-Escudé, J., Haehnelt, M., & Rees, M. J. 2000, *ApJ*, 530, 1

Santos, M. G., Amblard, A., Pritchard, J., Trac, H., Cen, R., & Cooray, A. 2008, *ApJ*, 689, 1

Santos, M. G. & Cooray, A., 2006, *PRD* 74, 083517.

Santos, M. G., Cooray, A., Haiman, Z., Knox, L., & Ma, C.-P. 2003, *ApJ*, 598, 756

Shin, M.-S., Trac, H., & Cen, R. 2008, *ApJ*, 681, 756

Sokasian, A., Abel, T., Hernquist, L., & Springel, V. 2003, *MNRAS*, 344, 607

Sokasian, A., Yoshida, N., Abel, T., Hernquist, L., & Springel, V. 2004, *MNRAS*, 350, 47

Spergel, D. N. et al. 2007, *ApJS*, 170, 377

Totani, T., Kawai, N., Kosugi, G., Aoki, K., Yamada, T., Iye, M., Ohta, K., & Hattori T. 2006, *PASJ*, 58, 485

Tozzi, P., Madau, P., Meiksin, A., & Rees, M. J. 2000, *ApJ*, 528, 597

Trac, H. & Cen, R. 2007, *ApJ*, 671, 1

Trac, H., Cen, R., & Loeb, A. 2008, *ApJ*, 689, L81

Trac, H. & Pen, U.-L. 2006, *New Astronomy*, 11, 273

White R., Becker R., Fan X., & Strauss M. 2003, *AJ*, 126, 1

Wouthuysen, S. A., 1952, *AJ*, 57, 31.

Wyithe, J. S. B. & Loeb, A., 2003, *ApJ*, 586, 693.

Wyithe, J. S. B. & Loeb, A., 2007, arXiv:0708.3392

Xu, Y., 2006, “21cm forest” (in Chinese), B.Sc. thesis of Peking University, supervised by X. Chen and Z. Fan.

Yue, B., Ciardi, B., Scannapieco, E., Chen, X., 2009, “21 cm signal from the IGM and minihalos”, manuscript submitted to *MNRAS*.

Zahn, O., Lidz, A., McQuinn, M., Dutta, S., Hernquist, L., Zaldarriaga, M., & Furlanetto, S. R. 2007, *ApJ*, 654, 12

Zhang, J., Hui, L., & Haiman, Z. 2007, *MNRAS*, 375, 324

Zhang, B. & Mészáros, P. 2004, *Int. J. Mod. Phys. A*, 19, 2385